nature communications

Article

https://doi.org/10.1038/s41467-024-55619-7

Towards non-blinking and photostable perovskite quantum dots

Received: 22 April 2024

Accepted: 18 December 2024

Published online: 02 January 2025

Check for updates

Chenjia Mi[1,4], Gavin C. Gee[1,4], Chance W. Lander[1], Donghoon Shin[2], Matthew L. Atteberry[1], Novruz G. Akhmedov[1], Lamia Hidayatova[1], Jesse D. DiCenso[1], Wai Tak Yip[1], Bin Chen[2], Yihan Shao[1] & Yitong Dong[1,3]

Surface defect-induced photoluminescence blinking and photodarkening are ubiquitous in lead halide perovskite quantum dots. Despite efforts to stabilize the surface by chemically engineering ligand binding moieties, blinking accompanied by photodegradation still poses barriers to implementing perovskite quantum dots in quantum emitters. To date, ligand tail engineering in the solid state has rarely been explored for perovskite quantum dots. We posit that attractive intermolecular interactions between low-steric ligand tails, such as π-π stacking, can promote the formation of a nearly epitaxial ligand layer that significantly reduces the quantum dot surface energy. Here, we show that single $CsPbBr_3$ quantum dots covered by stacked phenethylammonium ligands exhibit nearly non-blinking single photon emission with high purity (~98%) and extraordinary photostability (12 hours continuous operation and saturated excitations), allowing the determination of size-dependent exciton radiative rates and emission line widths of $CsPbBr_3$ quantum dots at the single particle level.

Photonic-based quantum networks have the potential to paradigmatically change information sciences[1]. One essential element for photonic quantum networks is the quantum light source. $CsPbX_3$ (X = Cl, Br, I) perovskite quantum dots (QDs) are promising light-emitting materials because of their high photoluminescence (PL) quantum yield (QY), and facile syntheses[2–4]. Advances in the precise synthetic control over the size, shape, and composition[5–7] of these perovskite QDs have catalyzed the development of highly efficient LEDs[8–10], lasers[11], and quantum light sources[12,13]. Recently, single $CsPbX_3$ QDs were intensively studied to demonstrate their single photon emissions[14] with high brightness[15] and photocoherence[16]. However, research on exciton dynamics in single $CsPbX_3$ QDs to date has mainly focused on weakly confined nanocrystals because size-confined $CsPbX_3$ QDs generally exhibit poor photostability. Particularly, perovskite QDs show severe PL intermittency (often referred to as blinking) and photodegradation when their sizes are smaller than their exciton Bohr diameters[17,18]. This convolutes their exciton properties with defect-related dynamics and QD structural changes[19,20]. Therefore, improving the photostability of perovskite QDs is vital to reliable experimental studies of size-dependent structural-optical relationships in perovskites, including exciton PL lifetime, exciton–lattice coupling, and many-body interactions. This knowledge is crucial in consolidating our current theoretical models of band-edge excitons in perovskites[21–23] and guiding the design of high-fidelity QD-based quantum light emitters.

The insufficient photostability of small $CsPbX_3$ QDs relates to their labile surface lattices and strong quantum confinement. Since the scale of exciton-surface lattice interactions is inversely proportional to the volume of the QD, the optical properties of small $CsPbX_3$ QDs are more prone to surface defects. Existing surface defects can create centers for nonradiative recombination or trap photogenerated charge carriers from excitons and leave the QD charged[24]. Subsequently generated excitons in this charged QD will form trions that can undergo fast nonradiative Auger recombination and turn the PL of the QD OFF[25]. In

[1]Department of Chemistry and Biochemistry, The University of Oklahoma, Norman, OK 73019, USA. [2]Department of Chemistry, Northwestern University, Evanston, IL 60208, USA. [3]Center for Quantum Research and Technology, The University of Oklahoma, Norman, OK 73019, USA. [4]These authors contributed equally: Chenjia Mi, Gavin C. Gee. e-mail: Yitong.Dong-1@ou.edu

addition, photo-illumination can create additional defect states[26] and induce surface ligand detachment[27] on perovskite QDs. The defect-induced QD photoionization, nonradiative recombination, and photochemical surface changes are all associated with blinking and structural degradations in perovskite QDs[18,28,29].

To improve the photostability of $CsPbX_3$ QDs, their surface defects need to be well passivated, and their surface lattices need to be stabilized. While coating a wide-bandgap semiconductor shell can suppress blinking and photodarkening in II-VI QDs, such as CdSe[30], a well-established shelling protocol for highly ionic $CsPbX_3$ QDs has yet to be discovered. Instead of shelling, a nearly epitaxial ligand coverage is required for a defect-free and stable QD surface. Unfortunately, traditional ligands on $CsPbX_3$ QDs are under adverse solubilization equilibrium and thus only deliver sufficient surface coverage in concentrated QD colloids[31,32]. Consequently, when the colloidal QDs are diluted to ensure low QD density for single-particle studies, the ligands will be stripped along with ions comprising the QD surface, creating surface defects. Ligands with engineered binding moieties to enhance surface affinities have been developed to mitigate QD surface disintegrations. For example, charge-neutral Zwitter-ionic molecules were applied to weakly confined $CsPbBr_3$ QDs to mitigate the ionic metathesis during QD dilution[33–35]. Additionally, surface treatments using didodecyldimethylammonium bromide (DDABr) or phosphonic acids can passivate exposed Pb cations and thus improve the PLQY of $CsPbBr_3$ QDs[36,37]. Nevertheless, small-sized $CsPbX_3$ QDs immobilized in the solid state still suffer from blinking and photodarkening[17,38], suggesting that their surfaces are still unstable under photoexcitation. While tolerated by weakly confined perovskite QDs, under-passivated surfaces or photogenerated defects can be detrimental to strongly confined QDs (Supplementary Note 1 and Supplementary Fig. 1)[9].

The cause of incomplete and unstable defect passivation lies within the intermolecular interaction in bulky ligands that cohered on QD surfaces in the solid state[39]. These ligands contain long hydrocarbon tails required to impart sufficient miscibility of ionic QDs with non-polar solvents. Furthermore, designer ligands often adopt branched or multiple hydrocarbon ligand tails to entropically promote the colloidal stability of QDs[33,40]. However, the effect of ligand tails when QDs are immobilized in the solid state has rarely been considered. The steric repulsion of bulky tails can negatively affect surface stability in the solid state. For example, DDA, a well-established ligand for colloidal $CsPbBr_3$ QDs, has two long-chain tails. But fully passivating the (100) facet of $CsPbBr_3$ using DDA would require an aliphatic chain density of ~5.7 chains·nm^{-2}, exceeding that of the crystalline aliphatic chain density (4.9 chains·nm^{-2})[41]. Therefore, bulky aliphatic ligand tails stabilizing QDs in solution are unlikely to accommodate complete and stable surface passivation of single $CsPbBr_3$ QDs in the solid state.

Reducing the steric hindrance of ligands can promote ligand access to QD surfaces. Since halide vacancies on the QD surface are proven optical traps[36], excess small ligand molecules containing halides can repair the QD surface and improve the PLQY. Previously, we aimed to supply excess ammonium bromides using small-sized ligands to enhance the PLQY of single $CsPbBr_3$ QDs[42]. By immersing the n-butylammonium bromide (NBABr) treated QDs in a small amount of saturated phenethylammonium bromide (PEABr) solution followed by heating, surface halide vacancies on the $CsPbBr_3$ QDs were efficiently filled, resulting in QDs with suppressed trion-induced blinking. This allowed us to discover a biexciton-like Auger blinking mechanism in strongly confined QDs at increased excitation intensity. However, the QD PL intensity still fluctuates, and the resistance to photodarkening was not demonstrated. This suggests that simply reducing the ligand steric effect is inadequate. Instead, we posit that the attractive inter-ligand-tail interaction is a critical yet missing factor toward non-blinking and photostable perovskite QDs.

In this work, we focus on studying the impact of ligand tail stacking on the photostability of $CsPbBr_3/I_3$ QDs in the solid state. Using density function theory (DFT) calculations and a combination of low-frequency Raman and single QD PL spectroscopies, we demonstrate that attractive π−π interaction between PEA ligand tails can significantly reduce the QD surface energy in the solid state and the degree of ligand tail stacking is critical to achieving nearly non-blinking and photostable QDs. Ligands on strongly confined $CsPbBr_3/I_3$ QD surfaces with long-chain tails are thoroughly exchanged with PEA using a solution-engineering method that promotes ligand tail stacking. Our single QDs exhibit nearly non-blinking PL emissions with high single photon purities (~98%). Furthermore, the stabilized surface lattices endow QDs with unprecedented photostability: they remain nearly blinking-free and photodarkening-free during 12 h of continuous laser irradiation and can sustain excitations at saturation intensities. These advantages enable the determination of size-dependent exciton radiative rates and emission linewidths of $CsPbBr_3$ QDs at the single-particle level.

Results

Impact of quantum dot ligand tails in the solid state

To understand the effect of the ligand tails on the surface ligand coverage of perovskite QDs in the solid state, we used DFT to estimate the surface energies of a DDA (truncated to reduce computation cost) passivated and a PEA passivated $2 \times 2 \times 1$ $CsPbBr_3$ slabs (Fig. 1a, b) as a function of surface ligand coverages (Supplementary Notes 2, 3 and Supplementary Figs. 2–6). Considering that the bulky ligand tails in DDA will lose conformational freedom during solidification, the intramolecular entropy reduction can significantly increase the surface energy (Supplementary Note 4). As shown in Fig. 1c, the lowest surface energy of the $CsPbBr_3$ slab was achieved when 7 of the 8 Cs^+ sites were filled by DDAs, while adding an additional DDA would increase the surface energy. This suggests that the ligand-to-ligand interactions can destabilize the surface passivation (Supplementary Note 5), which is in good agreement with previous studies[43]. To better visualize the effect of intermolecular interactions, we investigated the differential in surface energy regarding the numbers of surface ligands (Fig. 1c, d) representing the energy gain/loss of binding the Nth ($N = 1$–8) ligand onto the surface. It is seen that after the fourth DDA (50% surface coverage), additional DDA bindings were less energetically favored, and the eighth DDA binding was energetically forbidden. Therefore, complete surface passivation with bulky, entropic ligand tails can destabilize QD surfaces in the solid state.

This problem can be solved by reducing the size of ligand tails and functionalizing them with moieties featuring attractive intermolecular interactions. To assess the effect of such tail groups, we replaced truncated DDA cations with PEA cations, a small ligand that feature attractive intermolecular π-π stacking (Fig. 1b). First, the surface free energy reached the minimum when the surface is fully covered by PEAs (Fig. 1d). In addition, shorter ligand tails reduced the entropy penalty, and the surface free energy was much lower than that of the DDA-covered surface. Furthermore, the differential surface free energy of the PEA-covered QD slab indicated that increasing PEA coverage would always be favored. This suggests that the intermolecular π-π interaction between PEA cations can drive the near-epitaxial surface passivation of the QD surface and significantly reduce the QD surface energy, minimizing the probability of defect formations.

Our ligand design was then tested using strongly confined $CsPbBr_3$ QDs synthesized following a previously reported method with modifications (Methods)[5]. The QDs have a cubical shape and expose mostly the (100) facets (Fig. 1e and Supplementary Figs. 7, 8, PLQYs of the colloidal QDs are provided in Supplementary Table 1) passivated by oleylammonium ligands (the original ligands). PEAs attached on other facets such as (110) and (111) are unlikely to stack very well due to the larger distances between binding sites. We first investigated the π-π interaction between the bound PEA ligands using nuclear magnetic resonance (NMR) Overhauser effect spectroscopy (NOESY) for

https://doi.org/10.1038/s41467-024-55619-7

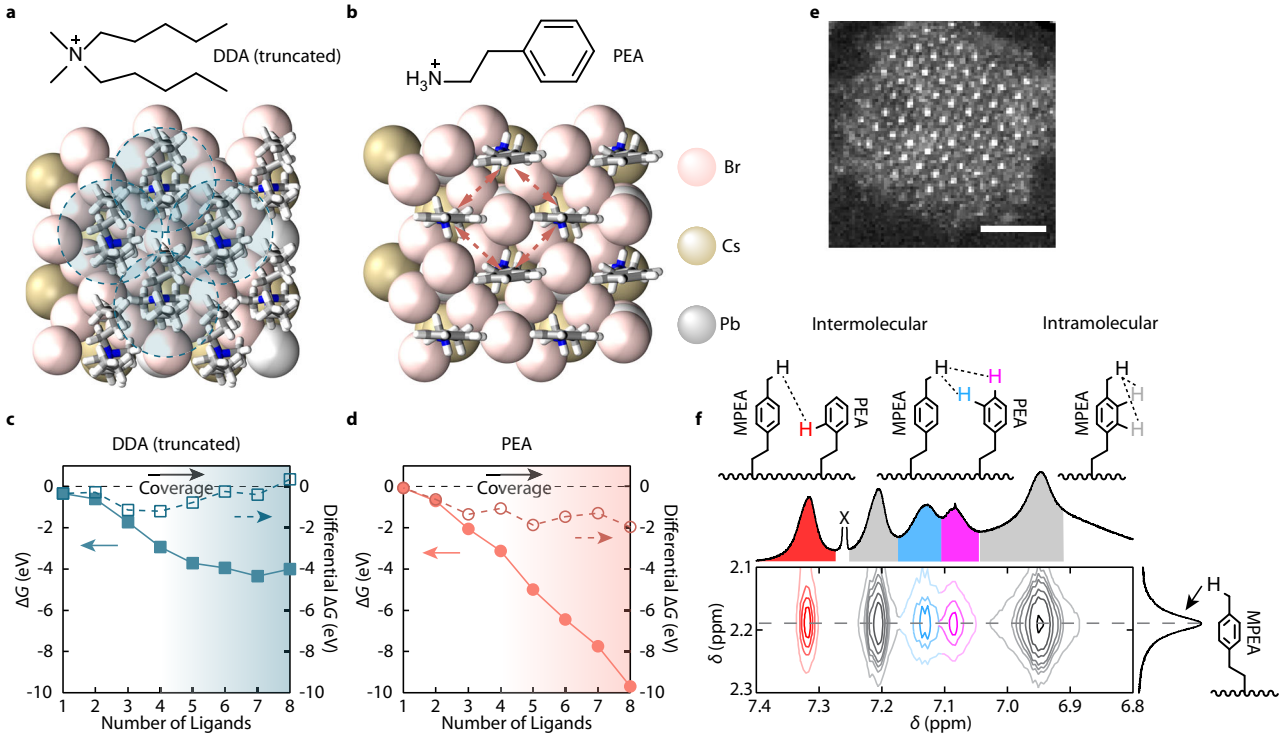

Fig. 1 | Free energies of ligand-covered $CsPbBr_3$ QD surfaces and intermolecular interactions of PEA ligands. a, **b** Slabs of $CsPbBr_3$ fully passivated with **a** DDA (truncated) and **b** PEA used in DFT calculations. The shaded circles in **a** indicate the intermolecular steric repulsions, while the dashed arrows in **b** indicate the intermolecular π-π stacking interactions. **c**, **d** Calculated surface free energies (solid marks) and differential free energies (hollow marks) as a function of the numbers of surface-bound **c** truncated DDA and **d** PEA ligands. Δ*G* represents free energy. The shadings indicate the ligand density. **e** STEM image of a strongly confined $CsPbBr_3$ QD exhibiting cuboidal shape, exposing mostly the (100) facets. The scale bar represents a length of 2 nm. **f** Expanded region of the solution NOESY spectrum shows QDs ligand-exchanged with mixed ligands containing PEABr and MPEABr, measured at 60 °C. *δ* represents chemical shift. The intermolecular (red, blue and purple) and intramolecular (gray) proton nOe correlations between PEA moieties on the QD surface are colored in both the schemes and the spectrum. The peak (partially unshown) marked by X is the chloroform solvent residue. The full spectrum is provided in Supplementary Fig. 11.

partially PEA-exchanged QD colloids. To prepare such QD colloids, a small amount of saturated PEABr *N*,*N*-dimethylformamide (DMF) solution was added into the QD colloids followed by purification (Methods). The ^{1}H NMR spectra showed that both PEA and oleylammonium cations were bound to the QDs (Supplementary Figs. 9, 10). The incomplete exchange was expected due to the limited solubility of PEABr in non-polar organic solvents. NOESY was used to monitor the coupling of protons on the surface-bound PEA phenyl rings. To distinguish the nOe signals contributed by intermolecular π−π stacking from the intramolecular coupling, half of the PEAs used for the ligand exchange were labeled by a methyl group on the *para* position of their phenyl rings (MPEA). Figure 1f shows the expanded region of the NOESY spectrum of the ligand-exchanged $CsPbBr_3$ QD colloids (full spectrum in Supplementary Fig. 11). Strong cross-peaks at 7.09, 7.13, and 7.32 ppm arose from the intermolecular correlations between the *para*-, *meta*-, and *ortho*-protons on the PEA phenyl rings and the *para*-methyl protons on the MPEA, respectively. This verifies the strong tendency of π−π stacking between the phenyl rings in surface-bound PEA ligands.

An approach to address the incomplete surface ligand exchange using solubility-incompatible ligands is solid-state ligand exchange, in which QDs capped by original ligands were exposed to a small volume of polar solutions containing shorter ligands[44]. However, QDs in a densely packed thin film typically used in the solid-state exchange cannot be optically resolved. To make QD samples for single-particle studies, we modified the solid-state ligand exchange by employing the solvent-engineering method[45,46]. Briefly, diluted $CsPbBr_3$ QDs were dripped onto a supersaturated PEABr solution in DMF on a spinning substrate (details in Methods). The QD solution acts as the anti-solvent to facilitate the removal of the host solvent (DMF) and to initialize the crystallization of PEA ligands with QDs. QD dilution helps the detachment of original ligands, and the low QD concentration also increases the PEA-to-QD ratio, which is critical for thorough ligand exchange[44]. As reported in our previous study[42], the high bromide concentration can facilitate the repair of anion vacancies on the QD surface and support the intrinsic electronic structure of $CsPbBr_3$, increasing the PLQY[36,47]. After the exchange, the sample was carefully annealed in a nitrogen glovebox to assist intermolecular stacking (Methods). It is worth mentioning that the QD morphology and solution-engineering ligand exchange parameters, such as QD dripping time and spin-coating parameters, are important in achieving PEA stacking (details discussed later). After the exchange, the PEA-covered QDs were dispersed in a crystalized matrix formed by excess PEABr molecules, as demonstrated in X-ray diffraction patterns (Supplementary Fig. 12). The NMR spectra of digested PEA-exchanged QDs show no signal from original ligands, suggesting high efficiency of the solution-engineering ligand exchange approach (Supplementary Fig. 13). Also, QDs in the PEABr matrix retained their cubical shape, suggesting the structural integrity of QDs is preserved during the solution-engineering ligand exchange (Supplementary Figs. 7, 8).

Blinking behaviors of single $CsPbBr_3/I_3$ quantum dots

We then studied the blinking behaviors of single $CsPbBr_3$ QDs (~4.5 nm) passivated by PEA through the solution-engineering ligand exchange (Fig. 2a, b). The same QDs were also ligand-exchanged to DDA in the colloidal phase and dispersed in a polymer matrix using a reported method[17] for comparison (Fig. 2c, d). It is worth noting that applying our solution-engineering ligand exchange method using DDA

https://doi.org/10.1038/s41467-024-55619-7

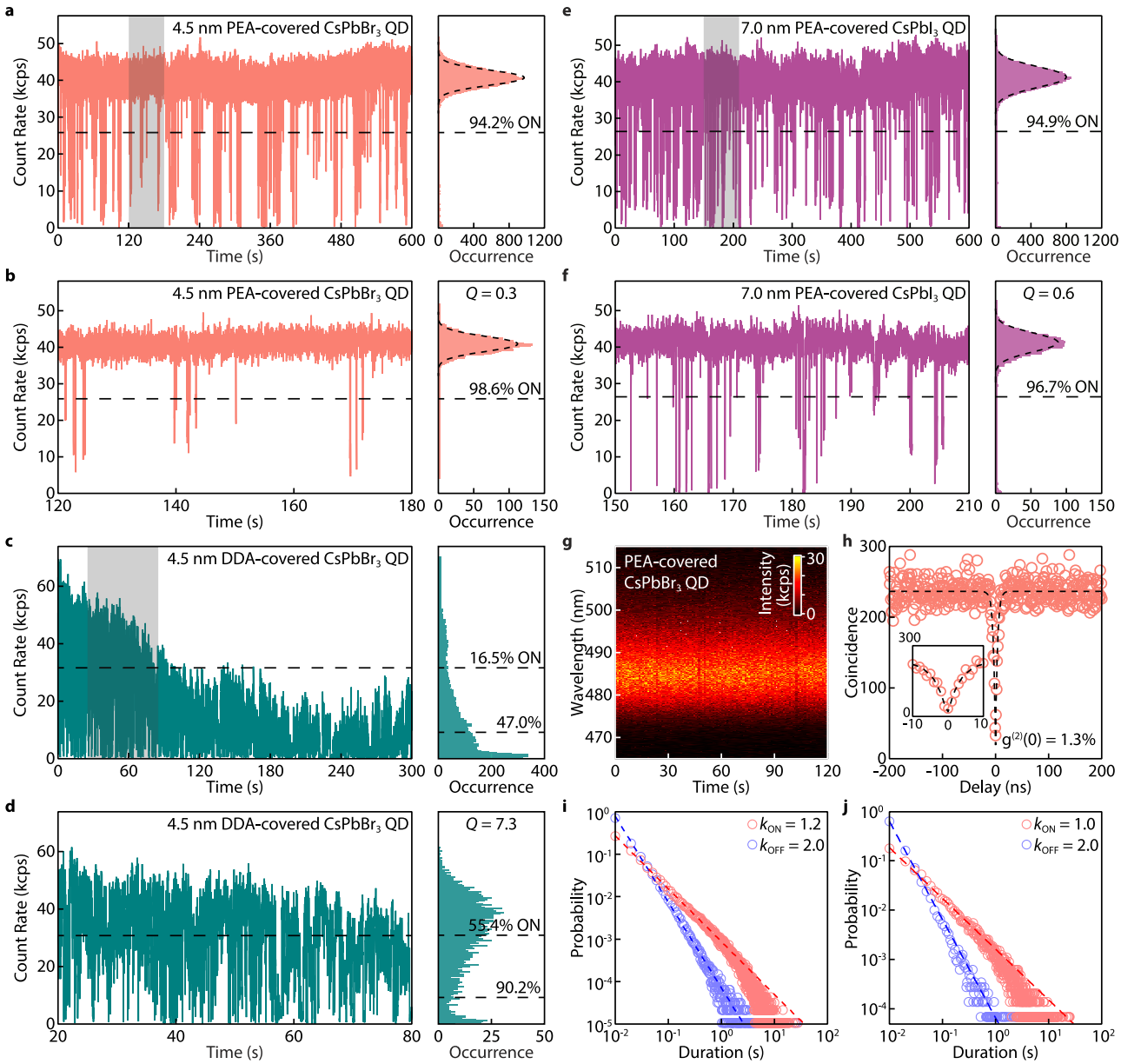

Fig. 2 | Nearly non-blinking strongly confined single $CsPbBr_3$ and $CsPbI_3$ QDs. **a**–**f** PL blinking traces and intensity distribution histograms of **a**–**d** two ~4.5 nm $CsPbBr_3$ QDs and **e**, **f** a ~7.0 nm $CsPbI_3$ QD, respectively. **a** and **e** show QDs covered by PEA and measured for 10 min. **b**, **f** show zoomed-in views of the blinking traces with a 1 min window indicated by the shaded areas in **a** and **e**, respectively. The intensity distribution histograms of **a, b**, **e**, **f** are shot-noise limited with a *Q* parameter of 0.3 and 0.6 for **b** and **f**, respectively. The distributions are fitted by Poissonian functions (dashed curves). **c** Shows a QD covered by DDA and dispersed in polystyrene, measured for 5 min. **d** Shows a zoomed-in view of the blinking traces with a 1-min window indicated by the shaded area in (**c**). All blinking traces were built using a bin time of 10 ms. The unit kcps represents kilo-counts per second. **g** Time-resolved PL spectra of a PEA-covered $CsPbBr_3$ QD. No PL intensity fluctuation or spectral diffusion are detected. **h** Second-order correlation ($g^{(2)}$) function of the QD in **b** fitted (dashed curve) to yield a $g^{(2)}(0)$ value of 1.3%. Inset is a zoomed-in view of the $g^{(2)}$ function near zero delay time. All QDs were excited by a 405 nm laser with *cw* mode with an intensity of 42 W cm^{-2} for $CsPbBr_3$ and 20 W cm^{-2} for $CsPbI_3$. **i**, **j** Probability distribution of the ON (red)/OFF (blue) durations obtained from the blinking trace of **i** a single ~5.5 nm $CsPbBr_3$ QD continuously measured over 10 h and **j** blinking traces of 60 individual $CsPbBr_3$ QDs measured over 60–300 s, fitted to a power-law distribution (dashed lines). $k_{ON/OFF}$ represents the corresponding power-law exponents extracted from the fits.

will compromise the integrity of QDs (Supplementary Fig. 14). Typically, the PL OFF state intensity threshold was determined by the QY of trions, which was usually smaller than 20% of the maximum PL intensity for $CsPbBr_3$ QDs[48,49], and the PL emissions with intensities above the OFF threshold were all considered the ON state. However, PL from this so-called ON state cannot properly represent pure excitonic emissions, since the frequent PL intensity fluctuation in $CsPbBr_3$ QDs[42], together with photodarkening, can convolute the PL from dimmer emissive states (e.g., gray states) with the PL from the excitonic state[50,51]. To better quantify the ON state fraction, the ON/OFF state threshold was raised to 50% of the maximum PL intensity in this work. As shown in Fig. 2c, d, the DDA-covered $CsPbBr_3$ QD exhibited severe PL blinking and experienced photodarkening after only 120 s of excitation. For measurements with a duration of 300 and 60 s, the DDA-covered QD exhibits a 16.5 and 55.4% ON time fraction, respectively. Despite the aggressive threshold, the PEA-covered QD remained mainly in the ON state without photodarkening over 10 min (Fig. 2a). Figure 2b shows a blinking trace in a 60 s time window. Specifically, the QD exhibited an ON time fraction of 94.2% over 10 min and 98.6% over 60 s, much higher than that of the DDA-covered QD.

https://doi.org/10.1038/s41467-024-55619-7

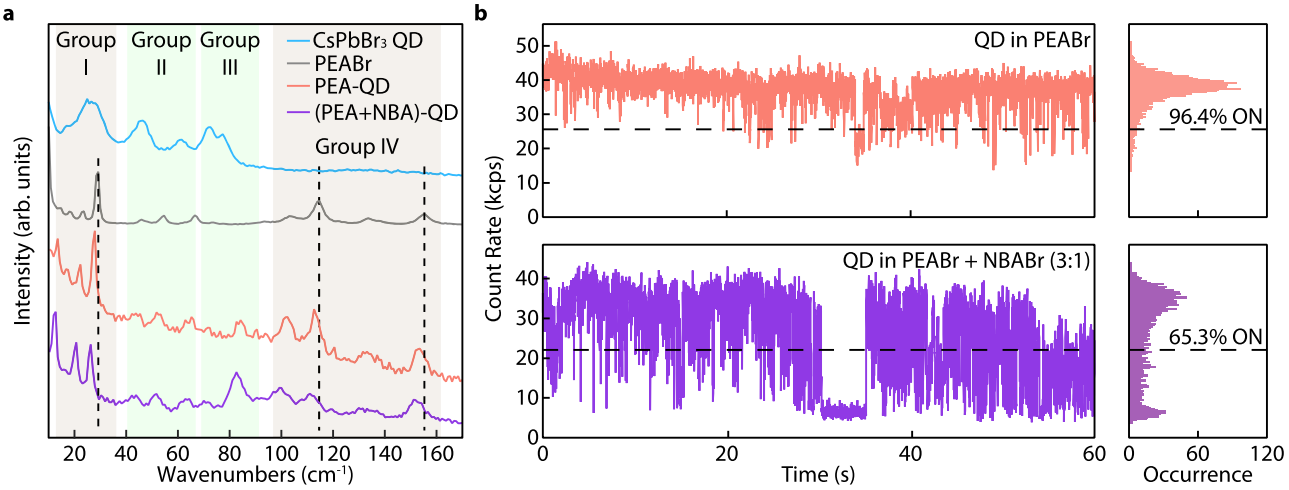

Fig. 3 | Effect of π-π stacking of PEA ligands on QD blinking. a Low-frequency Raman spectra of $CsPbBr_3$ QDs covered by the original ligands (oleylammonium, blue), pristine PEABr polycrystalline thin film (gray), PEA-covered $CsPbBr_3$ QDs (red), and $CsPbBr_3$ QDs after solution-engineering ligand exchange using a mixture of PEABr and NBABr (3:1 mass ratio, purple), measured at 77 K. **b** Blinking traces of single 4.3 nm $CsPbBr_3$ QDs covered by PEA (red) and PEA + NBA (3:1 mass ratio, purple). The blinking traces were built using a bin time of 10 ms. The unit kcps represents kilo-counts per second.

To better analyse the PL intensity trajectories of our PEA-covered $CsPbBr_3$ QD, we also used the Mandel Q parameter to quantify the deviation of the PL intensity distribution from shot-noise limited Poisson statistics (Supplementary Note 6)[51,52]. The PL intensity distribution of a nearly blinking-free QD should simultaneously have a high ON time fraction and a close-to-zero Q parameter. In Fig. 2d, DDA-covered QDs exhibited a broad and asymmetric PL intensity distribution histogram with a Q parameter of 7.3. In stark contrast, the PEA-covered QD exhibited a narrow PL intensity distribution with a Q parameter of 0.3. The ON time fraction and Mandel Q parameter of the PEA-covered QD remained consistent when a shorter bin time was used (Supplementary Fig. 15). These suggest that the PL emissions from the PEA-covered QD were dominated by exciton radiative recombination and were not influenced by stochastic QD charging or environmental charge redistributions. Our PEA passivation can also be applied to $CsPbI_3$ QDs by replacing PEABr with PEAI. The resulting QD exhibits a 94.9% ON time fraction with a Q parameter as small as 0.6 (Fig. 2e, f, PL spectrum and second-order correlation function in Supplementary Fig. 16).

Another consequence of charging-induced PL blinking is spectral diffusion and drifting, frequently reported in long-chain ligands covered by $CsPbBr_3$ QDs[16,33]. Such PL energy jumping and shifting are detrimental to the performance of QDs as quantum emitters. Our PEA-covered QD shows a spectrally stable PL. As shown in Fig. 2g, no spectral diffusion/jumping over 2.5 meV induced by QD charging was detected (the spectral diffusion detection is limited by the instrument energy and time resolution, 2.5 meV and 1 s), consistent with the nearly non-blinking behavior. In comparison, the DDA-covered QD showed clear spectral diffusion/jumping in the first 10 s of the measurement (Supplementary Fig. 17). The high single photon purity of the PEA-covered QDs with a $g^{(2)}(0)$ value of 0.013 for the $CsPbBr_3$ QD (Fig. 2h) was also expected, given their strong size confinement[12,13]. These are among the lowest $g^{(2)}(0)$ values reported for perovskite QDs (Supplementary Tables 2, 3).

This significantly improved single QD optical performance was echoed by the ON and OFF durations extracted from the blinking trace of a PEA-covered QD measured for 10 hours (Fig. 2i). The probability distributions for the duration (t) of the ON and OFF events, $P_{ON/OFF}$, were fitted to a power-law distribution $P \propto t^{-k_{ON/OFF}}$, where $k_{ON/OFF}$ were set as the power-law exponents that describe the statistics of the ON/OFF events. A smaller k_{OFF} (a steeper slope in the log-log plot) means long-duration OFF events were less likely to happen. In typical QDs, both k_{ON} and k_{OFF} values are ~1.5[53]. Our QDs showed an average k_{ON} of 2.0 and k_{OFF} value of 1.2, comparable to one of the best non-blinking core-shell II-VI and III-V QDs reported[30,54]. Additionally, statistics of ON and OFF durations from blinking traces of 60 PEA-covered $CsPbBr_3$ QDs were built (Fig. 2j). The high k_{ON} and low k_{OFF} suggest that most $CsPbBr_3$ QDs covered by PEA are almost defect-free, implying the high-effectiveness of the PEA solid-state passivation.

Effect of ligand tail π-π stacking on quantum dot blinking

The attractive π-π stacking is critical to achieving the nearly non-blinking QDs. QDs covered by ligands with only low-steric tails but without π-π stacking effects, such as iso-propylammonium (IPA) bromide, still showed a relatively low average ON time fraction of 83% (extracted from measurements of 67 IPA-covered QDs, Supplementary Fig. 18), implying the existence of surface defects due to incomplete passivation in IPA-covered QDs. Additionally, the QDs in our previous study[42] using PEABr to fill surface bromide vacancies without ligand tail engineering exhibited a 78% ON time fraction (using the ON/OFF threshold in this work) under moderate excitation, similar to that of IPA-covered QDs. The Q parameter of 8.9 was also much higher than that of our nearly non-blinking QDs covered by stacked PEA. This suggests that ligand tail engineering is critical to achieving nearly non-blinking behaviors in QDs.

To further understand the effect of π-π stacking on QD blinking behaviors, we have deliberately introduced NBA during the PEA solution-engineering ligand exchange (Methods and Supplementary Note 1). The intercalation of alkane chains will interfere with the aromatic stacking and reduce the intermolecular stacking effect in the molecular crystal matrix. The extent of PEA stacking and its impact on QDs are characterized using ultra-low frequency micro-Raman spectroscopic measurements at 77 K (Fig. 3a). The vibrational modes of PEABr crystal below 160 cm^{-1} are cataloged as intermolecular lattice vibrations of molecular crystals mixed with intramolecular modes[55–57]. The peaks attributed to PEA (groups I and IV) are significantly red-shifted when NBA is added, suggesting more spaced or disordered π-π stacking among PEAs. In contrast, the same groups of Raman peaks in the QD-in-PEA sample exhibit only minor shifts compared to the pristine PEABr crystalline thin film (with a high degree of π-π stacking, Supplementary Note 2). The disturbed π-π stacking in the PEA + NBA matrix is also corroborated by the linear absorption spectrum, manifested as a series of blue-shifted absorption peaks (Supplementary Fig. 19). In fact, the PEA ligand tail stacking is also very sensitive to QD

surface morphology and solution-engineering parameters and would not be achieved if the exchange process were not specifically optimized. This is supported by the blue-shifted and broadened absorption features of the PEA-QD sample reproduced using different spin-coating parameters and dripping times reported in our previous study (Supplementary Fig. 20).

The ligand tail stacking of PEA can potentially influence the QD lattices. Raman peaks from QDs are marked in group II between 40 and 70 cm^{-1} and group III between 70 and 90 cm^{-1}, corresponding to the Pb-Br bond bending modes and the octahedral distortions in perovskite[58–60]. While peaks in group II from the QD-in-molecular crystals are convoluted with lattice vibrations of PEA molecular crystals, the peak at ~82 cm^{-1} is distinct from the Raman modes of PEA. We tentatively attribute this peak to perovskite octahedral vibrations rigidified by the anchoring effects of stacked PEA ligands[61,62]. The corresponding QD blinking traces (Fig. 3b) clearly show that QDs are nearly non-blinking when covered by PEA ligands and start to blink when NBA interferes with the PEA stacking (additional blinking traces in Supplementary Fig. 21).

Photostability of quantum dots covered by stacking ligands

Similar to PL blinking, rapid photodegradation of $CsPbBr_3$ QDs has been a long-standing obstacle to investigating their excitonic properties at the single-particle level. Strongly confined $CsPbBr_3$ QDs are reported to experience spectral blue-shifting due to size-shrinking within a short time of laser excitation[13,63,64]. According to the DFT modeling, the QD surface can be significantly stabilized by stacking PEA ligands, which would manifest as resistance to photodegradation. Indeed, the single strongly confined $CsPbBr_3$ QD showed no size-shrinking-induced blue-shifting during 30 min of laser irradiation (Fig. 4a, b), and the PL spectra before and after the operation were nearly identical (Fig. 4c).

$CsPbBr_3$ QDs are notoriously prone to photodarkening. This occurs when photodegradation happens or light irradiation creates new surface defects on QDs and intensifies their PL blinking. Figure 4d, e show a strongly confined PEA-covered $CsPbBr_3$ QD that remains nearly non-blinking throughout a continuous photoexcitation of 10 h (additional blinking traces in Supplementary Fig. 22). Such continuous operation was also performed at an ensemble level. When a collection of isolated QDs were illuminated at the same time, their PL intensity stayed constant over the entire course of the measurement (>10 h, Fig. 4f). Notably, the PEA-covered QD remained nearly non-blinking with a 98% ON time fraction beyond 12 hours of continuous operation (Fig. 4g, h). In comparison, the PL intensity of QDs covered by DDA dispersed in polystyrene decreased since the first minute of laser exposure. Many QDs became nearly photobleached after ~10 min (Fig. 4f). QDs covered by IPAs, while showing improved photostability compared to DDA, experienced severe photodarkening (PL intensity dropped to 50% of the initial value) after ~10 min (Fig. 4f). QDs covered by PEAs prepared following the methods in our previous report[42], possessing inadequate ligand π-π stacking, also resulted in similar photodarkening behavior compared to those covered by IPAs (Supplementary Fig. 20). This further demonstrated the importance of attractive intermolecular interaction in ligands for solid-state QD passivation. Additionally, PEA-covered $CsPbI_3$ QD exhibits ~7 h of stable, nearly non-blinking continuous single photon emissions (Supplementary Fig. 23).

The photostability of single QDs under high excitation rates is critical to maximize the performance of SPEs. We also tested the stacked PEA-covered single QDs at high excitation intensities. As shown in Fig. 4i–l, PEA-covered $CsPbBr_3$ QDs remained nearly non-blinking when the excitation density (average number of excitons created per laser pulse, denoted as $\langle N \rangle$, see Supplementary Note 7) was close to saturation ($\langle N \rangle$ ~1). More blinking traces for QDs (including $CsPbI_3$) under high excitation rates (pulsed and *cw* excitation) are shown in Supplementary Fig. 24. In particular, $CsPbBr_3$ QD maintains > 90% ON time fraction over 15 min under oversaturated excitation densities ($\langle N \rangle = 2.0$, Supplementary Fig. 25). The extraordinary photostability results in a maximum overall single QD photon emission rate (~20 MHz for $CsPbBr_3$, ~40 MHz for $CsPbI_3$) approaching the physical limit (limited by the exciton lifetime, Supplementary Note 8).

In addition, PEA-covered QDs stayed nearly blinking-free for about a month of storage at ambient conditions (Supplementary Fig. 26). To the best of our knowledge, this is comparable to some of the most photostable non-blinking CdSe QDs with CdS shells[30]. Single QD samples without encapsulation also show stable PL spectra without significant changes in PL intensity after 24 h of exposure to the ambient environment (Supplementary Fig. 27). However, due to the hygroscopic nature of PEABr salts, single QD without encapsulation slightly blinks after 1 h of continuous operation and 24 h of ambient exposure (Supplementary Fig. 27).

Photoluminescence performance of $CsPbBr_3/I_3$ quantum dots

We then explored our ligand design on single $CsPbBr_3/I_3$ QDs with various sizes. The extent of quantum confinement in QDs increases with decreasing size, making the QDs more sensitive to surface defects. Rarely can a surface passivation method work effectively for QDs with different sizes. Figures 5a–f show blinking traces of four single $CsPbBr_3$ QDs and two single $CsPbI_3$ QDs covered by PEA with their sizes determined by their PL peak positions (Fig. 5g, h) using empirical sizing curves[6]. All QDs are nearly blinking-free with >94% ON time fractions and shot-noise-limited PL intensity distributions, suggesting that PEA epitaxially passivated the QD surfaces. Fluorescence lifetime-intensity distribution (FLID) plots of the $CsPbBr_3$ QDs show minimum PL intensity and lifetime fluctuations (Supplementary Fig. 28, additional single QD measurements are shown in Supplementary Fig. 29). Notably, weakly confined $CsPbBr_3$ QDs can also benefit from the surface PEA coverage: a single $CsPbBr_3$ QD with the size of 9 nm was nearly blinking-free and maintained a 94.1% ON time fraction over 30 minutes; no detectable spectral diffusion nor size-shrinking were detected during 1 hour of laser irradiation (Supplementary Fig. 30). We have also built statistics of PL properties extracted from 81 single $CsPbBr_3$ QD measurements, suggesting the overall effectiveness of our PEA passivation strategy (Supplementary Fig. 31).

Our QDs were then examined to study their biexciton dynamics (Fig. 5i, j). The fast biexciton Auger recombination of strongly confined $CsPbBr_3$ QDs is also echoed by a low average $g^{(2)}(0)$ value of 0.054 (Supplementary Fig. 31). We note that the variations of $g^{(2)}(0)$ values of nearly non-blinking QDs are smaller than QDs exhibiting PL intensity fluctuations (Supplementary Fig. 32)[13]. The larger $g^{(2)}(0)$ value variations in blinking QDs can be partially attributed to the attenuated single exciton emissions from other nonradiative channels (Supplementary Note 9). Our nearly non-blinking QDs are thus particularly useful for studying the biexciton recombination mechanisms since their $g^{(2)}(0)$ values can better represent the biexciton emission QY[65].

Size-dependent exciton properties at the single-dot level

Size-dependent exciton properties are fundamentally important for unraveling the PL emission mechanism and exciton–lattice interaction in QDs. Experimental determination of PL properties in single QDs excludes the interferences of ensemble inhomogeneity. However, blinking and photodarkening can change exciton dynamics and PL line shapes. The nearly non-blinking $CsPbBr_3$ QDs with significantly improved photostability are, therefore, ideal for studying the intrinsic effects of quantum confinement on excitons[66,67].

Exciton recombination dynamics were then studied using our single $CsPbBr_3$ QDs. They show mono-exponential PL intensity decay (Fig. 6a) due to the absence of dimmer emissive states. We extracted the PL lifetimes from 81 QDs with sizes ranging from 3.6 to 14 nm

https://doi.org/10.1038/s41467-024-55619-7

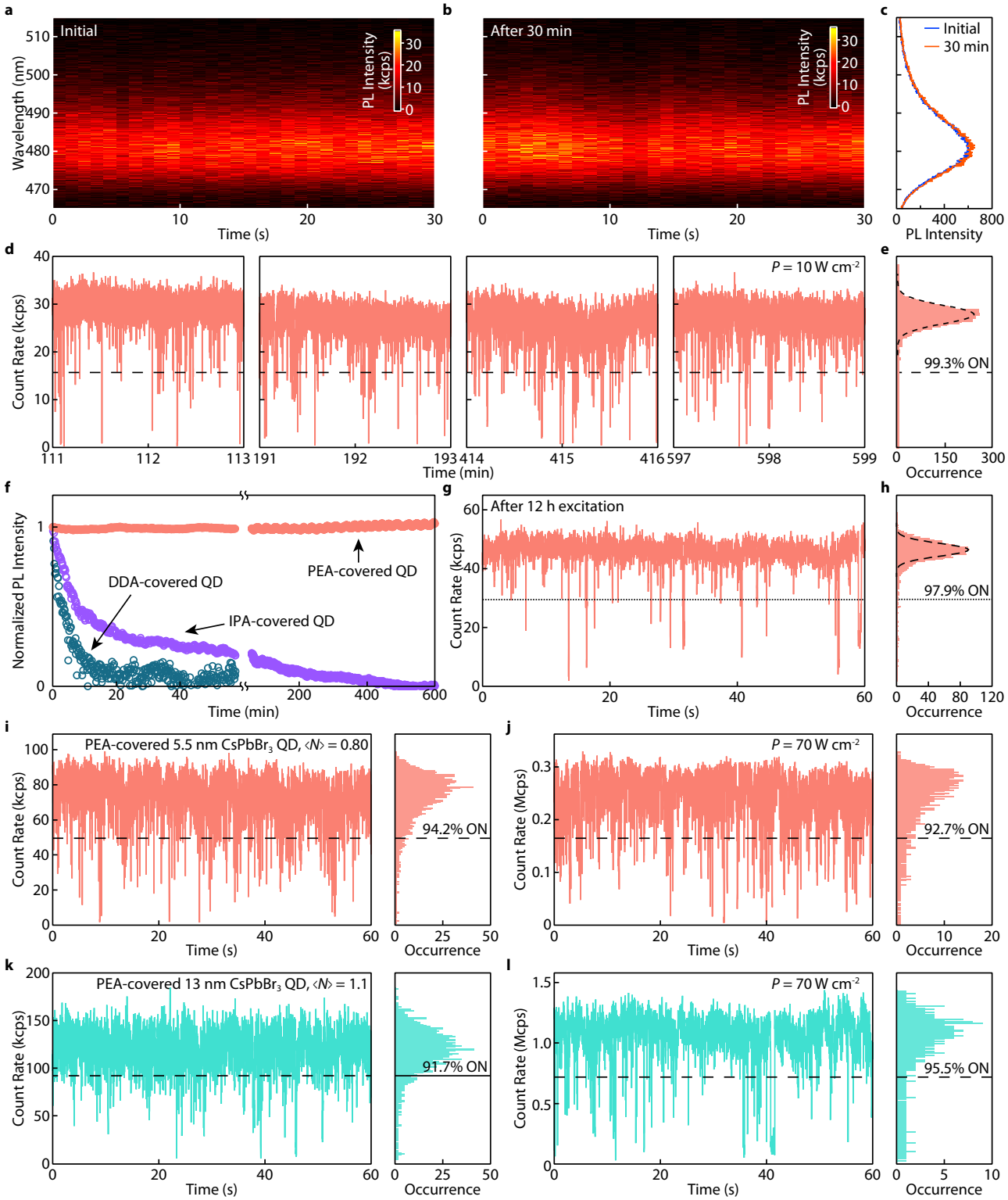

Fig. 4 | Spectral stability and resistance to photodarkening of PEA-covered $CsPbBr_3$ QDs. a, **b** Time-resolved PL spectra of a single $CsPbBr_3$ QD (~4.1 nm) **a** before and **b** after 30 min of continuous laser excitations (*cw* mode, 42 W cm^{-2}). **c** Integrated PL spectra from (**a**, **b**). The superimposed spectra showed no spectral shifting over 30 min of excitation. **d** Representative PL blinking trace segments extracted at different times of a single PEA-covered QD (~5.5 nm) continuously measured over 10 h (10 W cm^{-2}). **e** The PL intensity distribution histogram extracted from the last segment in **d**, showing the QD remained nearly non-blinking during the measurement. **f** Normalized PL intensity of a collection of PEA-covered $CsPbBr_3$ QDs (red) under 10 h of continuous laser excitation. In contrast, DDA-covered QDs (blue) and IPA-covered QDs (purple) were significantly photodarkened (50% of the initial PL intensity) in the first 3 min and 10 min of operation, respectively. **g** PL blinking trace and **h**, intensity distribution histogram of a single PEA-covered QD in **f** after 12 h of continuous operation. **i**–**l** PL blinking traces and PL intensity distribution histograms for two PEA-covered $CsPbBr_3$ QDs (**i**, **j** 5.5 nm and **k**, **l**, 13 nm), under intense laser excitation (**i**, **k**, pulsed mode, 2 MHz repetition rate, **j**, **l**, *cw*, excitation densities are noted in the figures), exhibiting very high count rates and >90% ON time fraction. All blinking traces were built using a bin time of 10 ms. The unit kcps represents kilo-counts per second, and the unit Mcps represents mega-counts per second.

https://doi.org/10.1038/s41467-024-55619-7

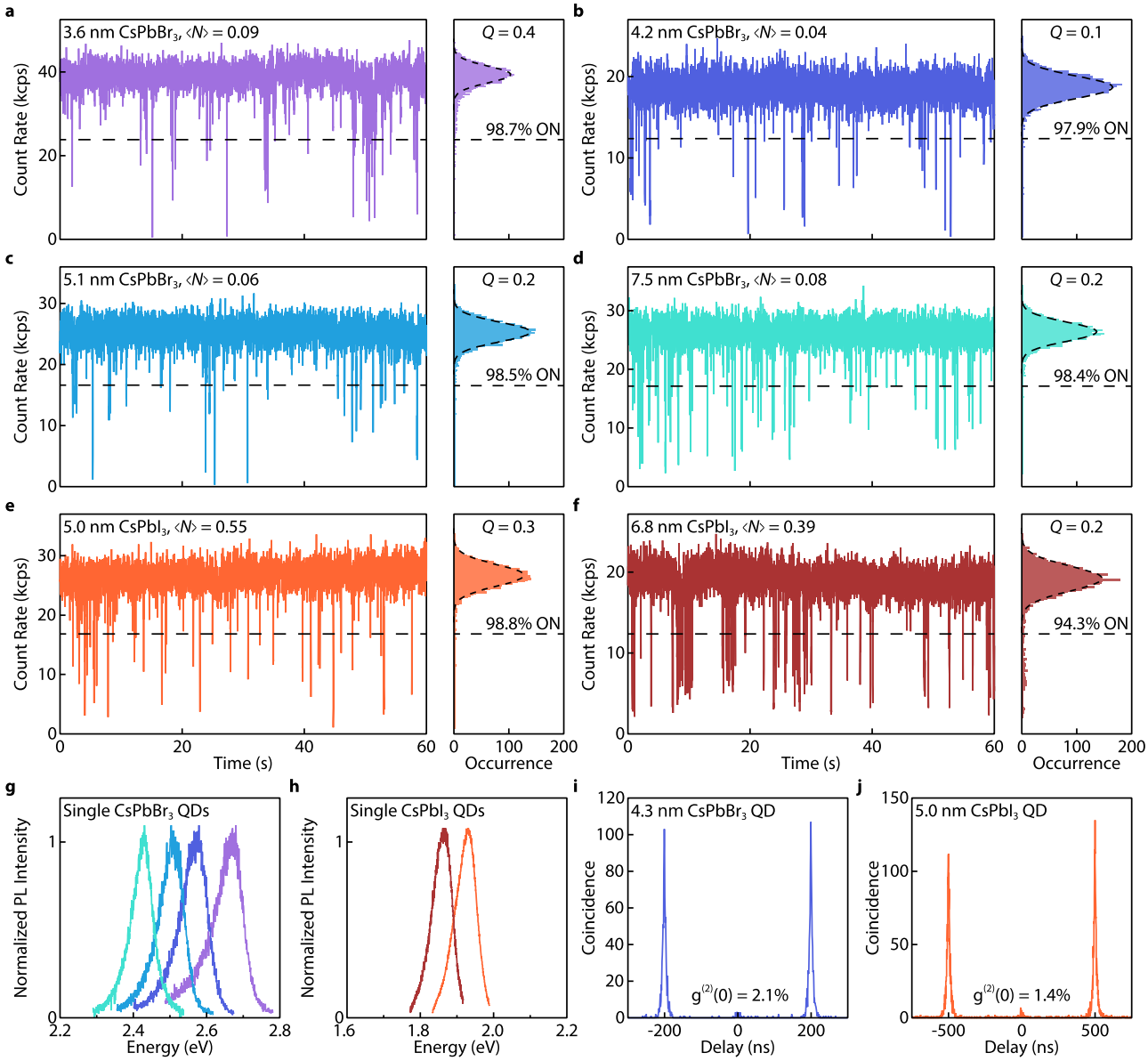

Fig. 5 | Nearly non-blinking PEA-covered $CsPbBr_3$ and $CsPbI_3$ QDs with various sizes. a–f Single QD PL blinking traces and intensity distribution histograms of **a–d** four PEA-covered $CsPbBr_3$ QDs and **e–f** two PEA-covered $CsPbI_3$ QDs with different sizes (405 nm pulsed laser excitation, 10 ms bin time). The intensity distribution histograms of all QDs are shot-noise limited (Poisson fits are superimposed, and *Q* parameters are provided). The unit kcps represents kilo-counts per second. **g, h** The corresponding PL spectra for the QDs. **i, j** Representative second-order correlation ($g^{(2)}$) plots of PEA-covered $CsPbBr_3$ and $CsPbI_3$ QDs, obtained under 5 and 2 MHz pulsed excitation, showing a $g^{(2)}(0)$ value of 2.1 and 1.4%, respectively.

(Fig. 6b). Interestingly, the size-radiative rate correlation appears not monotonic: the exciton radiative rate increases with reducing sizes and then decreases when the QDs are smaller than 4.5 nm. This is tentatively attributed to the combined effect of bandgap increasing and dark exciton state mixing on the apparent radiative recombination rate when QD size decreases (Supplementary Note 10). When QDs experience quantum confinement, the radiative rate scales with the increasing optical bandgap due to the increasing exciton oscillator strength[68–70]. When QD sizes decrease further, strong exchange interaction increases the energy gap between exciton fine structures comprising an optically active bright state and an optically dark state[23]. At room temperature, the PL lifetime measurement reflects radiative recombination from the thermally equilibrated bright state and ground dark state. A larger splitting between the bright and dark states will decrease the population of the bright states and thus result in a lower apparent recombination rate[67,68]. Non-monotonic size-radiative rate correlations are also observed in monodispersed colloids (Supplementary Fig. 33)[71]. However, only limited efforts have been made on the syntheses and characterizations of very small perovskite QDs, and the understanding of the size-radiative rate correlation requires more detailed experiments in the future.

Not only do our PEA-covered QDs reveal the exciton radiative rates, but they also exhibit intrinsic PL linewidths to help understand the size-dependence on exciton–lattice interaction in QDs. We discovered that the PL spectra were asymmetric for all $CsPbBr_3$ QDs even without spectral diffusion and shifting (Fig. 6c). We employed two Voigt functions with a common peak position to fit the single QD PL spectra. The half-width half-maximums (HWHMs) of both functions were extracted for 81 nearly non-blinking QDs (Fig. 6d). In the weakly confined region, our QDs showed similar or narrower PL peaks compared to reported values from other literature (Supplementary Fig. 34). With decreasing QD size, the PL linewidths increase

monotonically, which agreed well with previous studies[72]. However, the low-energy tail of the PL experienced a stronger dependence on the QD size compared to the high-energy part.

The low-energy tail in the PL spectrum of $CsPbBr_3$ QD ensembles was frequently observed but rarely studied. Bright band tail states were proposed to explain the asymmetric PL[73]. However, this would imply the existence of multiple dimmer emissive states compared to the exciton state and was inconsistent with the mono-exponential PL decay observed in our nearly non-blinking QDs. Asymmetric PL spectra have also been discovered in $CsPbBr_3$ polycrystalline films and have been attributed to the Cs^+ relocation[74]. However, this effect should not be evident at room temperature. The strong size-dependence of the low-energy tail infers that the surface lattices of the QDs may induce PL asymmetry. Thus, the intrinsic PL asymmetry can be related to the optical phonon sideband[75] or momentarily trapped exciton-polarons formed by exciton-surface lattice interactions, which were also found in 2D perovskite nanoplates[76]. This is supported by the spectrally independent PL decay dynamics of PEA-covered $CsPbBr_3$ QDs (Supplementary Fig. 35). Our study suggests that even for defect-free QDs, the size can still substantially affect exciton–lattice interactions.

In conclusion, we have demonstrated that intermolecular interactions can significantly impact the surface ligand coverage of individual $CsPbBr_3$ QDs in solid states. Although bulky long-chain ligand tails can entropically improve the colloidal stability of perovskite QDs, steric repulsion can lead to uncovered surface sites and ion loss. Considering the packing effect of the ligand tail in the solid state, we employed a low-steric ligand, PEA, with attractive intermolecular interactions on QDs, which was confirmed by the 2D NOSEY experiment. We demonstrated that the PEA-covered $CsPbBr_3$ and $CsPbI_3$ QDs were nearly non-blinking, with an average ON time fraction >90% and single photon emission purity reaching ~98%. Correlation between QD blinking behaviors and low-frequency Raman modes of PEA ligands in the solid state suggests that a high degree of π-π stacking between PEA ligands is critical to obtaining nearly blinking-free perovskite QDs. Furthermore, the QDs showed extraordinary photostability and remained nearly non-blinking after 12 h of continuous operation. Our PEA-covered $CsPbBr_3$ QDs enabled the determination of size-dependent excitonic properties without the interference of stochastic charging or photodegradation. The exciton radiative recombination rates and PL line shapes were measured as a function of QD size, providing insights into intrinsic exciton dynamics and exciton–lattice interaction in $CsPbBr_3$ QDs. Our study can benefit future fundamental studies on perovskite QDs at the single-particle level and potentially realize stable perovskite QD-based quantum emitters.

Methods

$CsPbBr_3$/I_3 quantum dot syntheses

To prepare the Cs-precursor, 900 mg Cs_2CO_3, 3.6 mL oleic acid (OA), and 9.6 mL 1-octadecnece (ODE) were added into a 100 mL flask. The mixture was vacuumed on a Schlenk line for 15 min while stirring. The mixture was then heated to 150 °C under vacuum until it turned clear. When the pressure reached ~1 Pa, the flask was filled with N_2. The temperature of the Cs-precursor was maintained at 120 °C for use.

The Pb-precursor was prepared by adding 600 mg $PbBr_2$, 1400 mg $ZnBr_2$, and 200 µL hydrobromic acid (48% w/w aq.) in a 250 mL flask. Then 14 mL OA, 14 mL oleylamine (OAm), and 40 mL ODE were added into the flask. The mixture was stirred vigorously for ~3 min and then vacuumed on a Schlenk line. The flask was then heated to 150 °C under vacuum until all solids were dissolved. The flask was then filled with N_2, and the solution temperature was adjusted to 80–150 °C according to the targeted size of the QDs. When the desired temperature for the Pb-precursor was reached, 4.5–5.0 mL of Cs-precursor solution (at ~120 °C) was injected into the Pb-precursor. The temperature of the solution was kept constant for 15–30 min. Controlling the Cs-precursor amount and reaction time favors the production of cubical-shaped QDs[77]. The crude product was then cooled to room temperature and transferred to centrifuge tubes for purification.

The crude product was first centrifuged at 7197 × *g* for 5 min. The precipitate was discarded. The supernatant was transferred to new centrifuge tubes, to which a 1:1 volume of acetone was added carefully and then shaken vigorously until the mixture turned turbid. This fast mixing was observed to help preserve the PLQY of the purified $CsPbBr_3$ QDs. The mixture was shaken until it became turbid. QDs were collected by centrifuging the mixture at 7197 × *g* for 5 min and discarding the supernatant. The precipitated QDs were redispersed in 5 mL hexanes to yield a stock $CsPbBr_3$ QD colloid. This stock colloid was further purified one to two times by reprecipitation with a 3:1 volume ratio of methyl acetate and redispersion with hexanes.

Larger strongly confined $CsPbBr_3$ QDs (6–7 nm) were synthesized with modified recipes: the amount of $ZnBr_2$ was increased to 2,000 mg, the reaction temperature was increased up to 200 °C and the reaction time was reduced to 1 min. Weakly confined $CsPbBr_3$ QDs (8–14 nm) were synthesized using previously reported methods with modifications[2]. In brief, a Pb-precursor solution was prepared by mixing containing 690 mg $PbBr_2$, 5 mL OA, 5 mL OAm, and 50 mL ODE in a 250 mL flask. The mixture was degassed and heated to 150–200 °C until a clear solution was formed. 1.15 mL of the Cs-precursor solution (described above, at ~120 °C) was swiftly injected into the Pb-precursor solution at 150–200 °C (for different targeted QD sizes) under the N_2 atmosphere. The reaction was quenched with an ice bath at 5 s after injection. The crude product was centrifuged at 7197 × *g* for 5 min, and the supernatant was decanted. The precipitate was redispersed in hexanes, and the resulting QD colloid was further purified one to two times by reprecipitation described above.

Strongly confined $CsPbI_3$ QDs were synthesized using a similar method as the $CsPbBr_3$ QDs with quantities of chemicals being tuned. Specifically, 125 mg Cs_2CO_3, 0.45 mL OA, and 4.45 mL ODE were used to prepare the Cs-precursor using the same procedure described above. To prepare the Pb-precursor, 120 mg PbI_2, 250– 500 mg ZnI_2 (for different targeted QD sizes), 2.5 mL OA, 2.5 mL OAm, and 5 mL ODE were mixed in a 25 mL flask, vacuumed on a Schlenk line, heated to 150 °C and maintained for 10 min until all solids were dissolved. Then the flask was filled with nitrogen and heated to 180 °C. About 0.4 mL of the Cs-precursor was swiftly injected into the reaction flask and allowed to react for 40 s. The reaction was then quenched to 50 °C with a water bath (to reduce the generation of the yellow phase $CsPbI_3$). The crude mixture was then purified by precipitation with a 3:1 volume ratio of methyl acetate and redispersion with hexanes. Further centrifugation (16,100×*g*) may be needed to remove the yellow phase $CsPbI_3$.

Solution ligand exchange of $CsPbBr_3$ quantum dots

About 404 mg PEABr (or 202 mg PEABr + 216 mg MPEABr) was dissolved in 1 mL DMF and filtered through a PTFE syringe filter (VWR, 0.22-µm pore size). About 2 mL $CsPbBr_3$ QD stock colloids (~100 µM) were reprecipitated two to three times with 10 mL methyl acetate and redissolved in 2 mL toluene or chloroform each time. To the purified $CsPbBr_3$ QD colloids, 40 µL of the PEABr DMF solution was added and vortexed for ~5 s. Then the mixture was centrifuged at 7197 × *g* for 1 min, and the supernatant was carefully transferred to a new centrifuge tube. To the supernatant, 10 mL of methyl acetate was used to reprecipitate the QDs. This procedure was repeated to promote ligand exchange. After two to three times of ligand exchange, the precipitate QDs were vacuum-dried for 20 min and then redissolved in 0.8 mL anhydrous $CDCl_3$ for NMR measurements.

Nuclear magnetic resonance measurements

The ^1H and NOESY NMR spectra were recorded on a VNMRS 500 MHz spectrometer at 25 °C and 60 °C equipped with a triple-resonance z-axis pulsed field gradient 5-mm probe. Typical parameters for acquiring ^1H NMR spectra were as follows: 8012.8 Hz spectral width,

https://doi.org/10.1038/s41467-024-55619-7

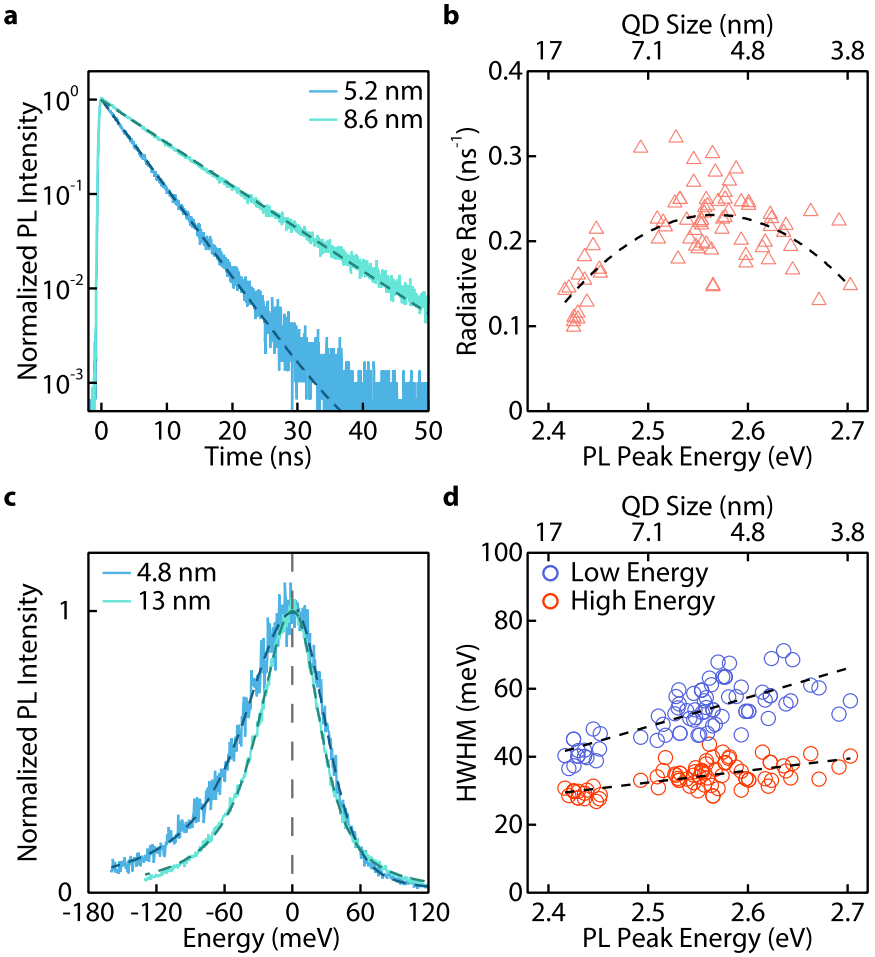

Fig. 6 | Size-dependent exciton properties of $CsPbBr_3$ QDs. a Representative time-resolved PL intensity traces of two single PEA-covered $CsPbBr_3$ QDs, exhibiting mono-exponential decay (dashed curves). **b** Statistics of exciton radiative recombination rates of 81 nearly non-blinking QDs with different sizes. A dashed curve is a visual guide. **c** PL spectra of two single PEA-covered $CsPbBr_3$ QDs (intensity-normalized and peak position-shifted to zero for comparison). Dashed curves are fits, each using two Voigt functions that share a common peak position for the asymmetric spectra. **d** PL linewidths (half-width half-maximum, HWHM, in the unit of milli-electron volt, meV) extracted from the high energy side and the low energy side of PL spectra for 81 nearly non-blinking QDs. Dashed lines are visual guides. The standard deviations are generally smaller than indicated by the size of the markers in (**b**, **d**).

5.0 s acquisition time, 4.5 µs (45°) pulse width, 1 s relaxation time, and 16 transients. The parameters for the NOESY were as follows: 5506.6 Hz spectral width in both dimensions (F1 and F2), 0.25 s acquisition time, 11.8 µs (90°) pulse width, 1.5 s relaxation time, 500 ms mixing time, 64 transients, with 512 increments along F1 dimension, each in phase-sensitive mode. The free induction decays (FIDs) were zero-filled to give a 2k × 2k data matrix, and a Gaussian function was applied in both dimensions (F1 and F2) prior to Fourier transformation. The FIDs of the ^{1}H and NOESY NMR spectra were processed using MNOVA. The ^{1}H NMR chemical shifts are assigned relative to the residual proton peaks of $CDCl_3$ at 7.26 ppm.

Solution-engineering ligand exchange

Glass coverslips (25 mm × 25 mm × 0.17 mm) were cleaned by sonicating in triton-X detergent solution, DI water, acetone, and 2-propanol sequentially (40 min each), and then dried. Before use, the coverslips were cleaned with a UV-ozone cleaner for 40 min and transferred to a nitrogen glovebox. In the glovebox, 200 mg PEABr was dissolved in 1 mL of anhydrous DMF and filtered through a PTFE syringe filter (VWR, 0.22 µm pore size). The stock QD colloid was diluted using anhydrous octane to ~200 pM. For the solution-engineering ligand exchange, 150 µL of the PEABr solution was spin-coated on a clean coverslip at 4000 rpm. After ~35 s (~15 s for larger QDs), 10 µL of the dilute $CsPbBr_3$ QD colloid was swiftly dripped on the coverslip while spinning. The extent of PEA stacking on QDs appears sensitive to the spin rate and QD dripping time, which were optimized in this work. Detailed QD size-dependent solution-engineering parameters are provided in Supplementary Fig. 36. The coverslip was then annealed on a hot plate at 50– 70 °C for 30–120 s. Then, the sample coverslip was covered by a glass slide. The gaps between the coverslip and the glass slide were sealed using UV-curing optical adhesives (Thorlabs NOA61). Other solution-engineering ligand-exchanged QDs, such as IPA-covered QDs and PEA-covered $CsPbI_3$ QDs, were prepared using similar protocols.

QD samples for linear absorption spectroscopy were prepared using the same spin-coating protocol on clean sapphire substrates (Φ 9 mm × 0.2 mm, c-axis, double-side polished). QD samples used for Raman spectroscopy and XRD were spin-coated on clean silicon substrates (10 mm × 10 mm × 0.5 mm, 100 facet polished) following the protocol above. Note that the concentration of the ligand (PEABr, etc.) solution used for solution-engineering ligand exchange was ~400 mg mL^{-1}, and the QD concentration was also increased to ~20 µM. The pristine molecular crystal samples and native-ligand QD samples were prepared by spin-coating corresponding ligand solutions directly onto proper substrates at 1000 rpm for 60 s. All these samples were

annealed/dried on a hot plate at 50–70 °C for 30–120 s, and then stored in sealed plastic tubes filled with dry nitrogen.

DDA-covered QDs were prepared following a reported method[17]. In brief, the solution ligand exchange was performed by adding 100 µL 0.01 M DDABr toluene solution to 1 mL of stock QD colloid and stirring for 1 h. Then, the QD colloid was diluted using a toluene solution of 0.1% (w/w) of polystyrene (average M.W. 260,000) to ~200 pM. Then 150 µL of the dilute solution was spin-coated on a clean coverslip at 3000 rpm for 60 s. The sample coverslip was then dried on a hot plate at 50 °C, and then encapsulated using UV adhesives following the same protocol used for PEA-covered QDs.

Single-dot spectroscopic measurements

The single QD sample was mounted onto a nano-positioner (Milles Griot Nanomax, with 3-axis manual and close-loop piezoelectric actuators) in a customized wide-field/confocal fluorescence microscope system (Supplementary Fig. 37). A 405 nm diode laser was used to excite the sample (Picoquant LDH-D-C-405, driven by a Picoquant Sepia PDL828 module) in either pulsed mode with a repetition rate of 2–5 MHz or *cw* mode. The laser was attenuated using a series of neutral density (ND) filters (Thorlabs) and sent into the objective lens (Olympus UPLXAPO100XO, 100× magnification, NA = 1.45) through a single-mode optical fiber (Thorlabs P1-305A-FC-1 with a collimator). The estimated focused laser beam diameter is ~475 nm. The excitation fluence was set to 0.4–30 µJ cm^{-2} for QDs with different sizes. For example, exciting a 4.3 nm $CsPbBr_3$ QD to $\langle N \rangle = 0.2$ requires an excitation power density of ~27.4 W cm^{-2} (or a fluence of 13.7 µJ cm^{-2}) using a 2 MHz repetition rate. The single QD sample was imaged using an EMCCD camera (Andor iXon Ultra 897) under wide-field mode. The QD of interest was moved to the center of the laser beam focus spot for spectroscopy measurements under confocal mode. PL emissions of a single QD was collected using the same objective and sent through a set of optical filters (a 405 nm notch filter, a 425 nm long-pass filter and optional bandpass filters). The QD PL spectra was measured using a spectrograph (Andor Shamrock 500i equipped with an Andor iXon Ultra 897 EMCCD). The time-tagged, time-resolved single photon counting (to generate the blinking traces, the time-resolved PL decay, and the second-order photon correlation) were recorded using two single-photon avalanche diodes (Hamamatsu C11202-100) connected to a time-correlator (Picoquant HydraHarp 400) in a Hanbury Brown and Twiss configuration. The $g^{(2)}(0)$ values were corrected using a previously reported method[65]. In brief, the background level was estimated from the PL decay traces, and its ratio to the total photon counts (usually 2.0%) was subtracted from the raw $g^{(2)}(0)$ value. All measurements were performed at room temperature.

Low-temperature, low-frequency Raman spectroscopy

Raman measurements were performed using a confocal Raman spectrometer (LabRAM HR Evolution, Horiba) equipped with a temperature control stage. The scattered Raman photons were dispersed using a 600 g cm^{-1} grating and collected by the spectrometer with a 633 nm laser, utilizing x10 and x50/VIS lenses. The laser power was regulated by an ND filter (10–25%) to avoid damaging the QD. For low-frequency Raman spectra, the instrument was equipped with an ultra-low frequency (ULF) module, allowing the acquisition of Raman signals in the spectral region below 200 cm^{-1}.

Density function theory modeling

The binding energy of ligands on the surface of $CsPbBr_3$ was calculated using DFT. The surface of the nanocrystal was modeled as a 2 × 2 × 1 (100) $CsPbBr_3$ slab. Details on the computational methodology can be found in Supplementary Note 2.

Data availability

The processed spectroscopic data are available at Figshare under accession codehttps://doi.org/10.6084/m9.figshare.27115519.

References

1. Kimble, H. J. The quantum internet. *Nature* **453**, 1023–1030 (2008).
2. Protesescu, L. et al. Nanocrystals of cesium lead halide perovskites ($CsPbX_3$, X = Cl, Br, and I): novel optoelectronic materials showing bright emission with wide color gamut. *Nano Lett.* **15**, 3692–3696 (2015).
3. Dey, A. et al. State of the art and prospects for Halide perovskite nanocrystals. *ACS Nano* **15**, 10775–10981 (2021).
4. Kovalenko, M. V., Protesescu, L. & Bodnarchuk, M. I. Properties and potential optoelectronic applications of lead halide perovskite nanocrystals. *Science* **358**, 745–750 (2017).
5. Dong, Y. et al. Precise control of quantum confinement in cesium lead halide perovskite quantum dots via thermodynamic equilibrium. *Nano Lett.* **18**, 3716–3722 (2018).
6. Akkerman, Q. A. et al. Controlling the nucleation and growth kinetics of lead halide perovskite quantum dots. *Science* **377**, 1406–1412 (2022).
7. Nedelcu, G. et al. Fast anion-exchange in highly luminescent nanocrystals of cesium lead halide perovskites ($CsPbX_3$, X = Cl, Br, I). *Nano Lett.* **15**, 5635–5640 (2015).
8. Kim, J. S. et al. Ultra-bright, efficient and stable perovskite light-emitting diodes. *Nature* **611**, 688–694 (2022).
9. Dong, Y. et al. Bipolar-shell resurfacing for blue LEDs based on strongly confined perovskite quantum dots. *Nat. Nanotechnol.* **15**, 668–674 (2020).
10. Jiang, Y. et al. Synthesis-on-substrate of quantum dot solids. *Nature* **612**, 679–684 (2022).
11. Ahn, N., Livache, C., Pinchetti, V. & Klimov, V. I. Colloidal semiconductor nanocrystal lasers and laser diodes. *Chem. Rev.* **123**, 8251–8296 (2023).
12. Park, Y.-S., Guo, S., Makarov, N. S. & Klimov, V. I. Room temperature single-photon emission from individual perovskite quantum dots. *ACS Nano* **9**, 10386–10393 (2015).
13. Zhu, C. et al. Room-temperature, highly pure single-photon sources from all-Inorganic lead halide perovskite quantum dots. *Nano Lett.* **22**, 3751–3760 (2022).
14. Zhu, C. et al. Single-photon superradiance in individual caesium lead halide quantum dots. *Nature* **626**, 535–541 (2024).
15. Hsu, B.-W. et al. Very robust spray-synthesized $CsPbI_3$ quantum emitters with ultrahigh room-temperature cavity-free brightness and self-healing ability. *ACS Nano* **15**, 11358–11368 (2021).
16. Utzat, H. et al. Coherent single-photon emission from colloidal lead halide perovskite quantum dots. *Science* **363**, 1068–1072 (2019).
17. Boehme, S. C. et al. Strongly confined $CsPbBr_3$ quantum dots as quantum emitters and building blocks for rhombic superlattices. *ACS Nano* **17**, 2089–2100 (2023).
18. Yuan, G. et al. The degradation and blinking of single $CsPbI_3$ perovskite quantum dots. *J. Phys. Chem. C.* **122**, 13407–13415 (2018).
19. Ahmed, T., Seth, S. & Samanta, A. Mechanistic investigation of the defect activity contributing to the photoluminescence blinking of $CsPbBr_3$ perovskite nanocrystals. *ACS Nano* **13**, 13537–13544 (2019).
20. Becker, M. A. et al. Unraveling the origin of the long fluorescence decay component of cesium lead halide perovskite nanocrystals. *ACS Nano* **14**, 14939–14946 (2020).
21. Becker, M. A. et al. Bright triplet excitons in caesium lead halide perovskites. *Nature* **553**, 189–193 (2018).
22. Tamarat, P. et al. The ground exciton state of formamidinium lead bromide perovskite nanocrystals is a singlet dark state. *Nat. Mater.* **18**, 717–724 (2019).

23. Sercel, P. C. et al. Exciton fine structure in perovskite nanocrystals. *Nano Lett.* **19**, 4068–4077 (2019).
24. Efros, A. L. & Nesbitt, D. J. Origin and control of blinking in quantum dots. *Nat. Nanotechnol.* **11**, 661–671 (2016).
25. Yuan, G., Gómez, D. E., Kirkwood, N., Boldt, K. & Mulvaney, P. Two mechanisms determine quantum dot blinking. *ACS Nano* **12**, 3397–3405 (2018).
26. Motti, S. G. et al. Photoinduced emissive trap states in lead halide perovskite semiconductors. *ACS Energy Lett.* **1**, 726–730 (2016).
27. An, R. et al. Photostability and photodegradation processes in colloidal CsPbI3 perovskite quantum dots. *ACS Appl. Mater. Interfaces* **10**, 39222–39227 (2018).
28. Darmawan, Y. A., Yamauchi, M. & Masuo, S. In situ observation of a photodegradation-induced blueshift in perovskite nanocrystals using single-particle spectroscopy combined with atomic force microscopy. *J. Phys. Chem. C.* **124**, 18770–18776 (2020).
29. Baitova, V. A. et al. Evolution of the luminescence properties of single $CsPbBr_3$ perovskite nanocrystals during photodegradation. *JETP Lett.* **118**, 560–567 (2023).
30. Chen, O. et al. Compact high-quality CdSe–CdS core–shell nanocrystals with narrow emission linewidths and suppressed blinking. *Nat. Mater.* **12**, 445–451 (2013).
31. De Roo, J. et al. Highly dynamic ligand binding and light absorption coefficient of cesium lead bromide perovskite nanocrystals. *ACS Nano* **10**, 2071–2081 (2016).
32. Almeida, G., Infante, I. & Manna, L. Resurfacing halide perovskite nanocrystals. *Science* **364**, 833–834 (2019).
33. Morad, V. et al. Designer phospholipid capping ligands for soft metal halide nanocrystals. *Nature* **626**, 542–548 (2024).
34. Krieg, F. et al. Stable ultraconcentrated and ultradilute colloids of $CsPbX_3$ (X = Cl, Br) nanocrystals using natural lecithin as a capping ligand. *J. Am. Chem. Soc.* **141**, 19839–19849 (2019).
35. Krieg, F. et al. Colloidal $CsPbX_3$ (X = Cl, Br, I) nanocrystals 2.0: zwitterionic capping ligands for improved durability and stability. *ACS Energy Lett.* **3**, 641–646 (2018).
36. Bodnarchuk, M. I. et al. Rationalizing and controlling the surface structure and electronic passivation of cesium lead halide nanocrystals. *ACS Energy Lett.* **4**, 63–74 (2019).
37. Zhang, B. et al. Alkyl phosphonic acids deliver $CsPbBr_3$ nanocrystals with high photoluminescence quantum yield and truncated octahedron shape. *Chem. Mater.* **31**, 9140–9147 (2019).
38. Paul, S., Kishore, G. & Samanta, A. Photoluminescence blinking of quantum confined $CsPbBr_3$ perovskite nanocrystals: influence of size. *J. Phys. Chem. C.* **127**, 10207–10214 (2023).
39. Boles, M. A., Ling, D., Hyeon, T. & Talapin, D. V. The surface science of nanocrystals. *Nat. Mater.* **15**, 141–153 (2016).
40. Yang, Y. et al. Entropic ligands for nanocrystals: from unexpected solution properties to outstanding processability. *Nano Lett.* **16**, 2133–2138 (2016).
41. Lüth, H., Nyburg, S. C., Robinson, P. M. & Scott, H. G. Crystallographic and calorimetric phase studies of the n-Eicosane, $C_{20}H_{42}$: n-Docosane, $C_{22}H_{46}$ system. *Mol. Cryst. Liq. Cryst.* **27**, 337–357 (1974).
42. Mi, C. et al. Biexciton-like Auger blinking in strongly confined $CsPbBr_3$ ferovskite quantum dots. *J. Phys. Chem. Lett.* **14**, 5466–5474 (2023).
43. Imran, M. et al. Simultaneous cationic and anionic ligand exchange for colloidally stable $CsPbBr_3$ nanocrystals. *ACS Energy Lett.* **4**, 819–824 (2019).
44. Kirmani, A. R., Walters, G., Kim, T., Sargent, E. H. & Amassian, A. Optimizing solid-state ligand exchange for colloidal quantum dot optoelectronics: how much is enough? *ACS Appl. Energy Mater.* **3**, 5385–5392 (2020).
45. Taylor, A. D. et al. A general approach to high-efficiency perovskite solar cells by any antisolvent. *Nat. Commun.* **12**, 1878 (2021).
46. Jeon, N. J. et al. Solvent engineering for high-performance inorganic–organic hybrid perovskite solar cells. *Nat. Mater.* **13**, 897–903 (2014).
47. du Fossé, I. et al. Limits of defect tolerance in perovskite nanocrystals: effect of local electrostatic potential on trap states. *J. Am. Chem. Soc.* **144**, 11059–11063 (2022).
48. Kanemitsu, Y. Trion dynamics in lead halide perovskite nanocrystals. *J. Chem. Phys.* **151**, 170902 (2019).
49. Yarita, N. et al. Dynamics of charged excitons and biexcitons in $CsPbBr_3$ perovskite nanocrystals revealed by femtosecond transient-absorption and single-dot luminescence spectroscopy. *J. Phys. Chem. Lett.* **8**, 1413–1418 (2017).
50. Qin, H., Meng, R., Wang, N. & Peng, X. Photoluminescence intermittency and photo-bleaching of single colloidal quantum dot. *Adv. Mater.* **29**, 1606923 (2017).
51. Malko, A. V. et al. Pump-intensity- and shell-thickness-dependent evolution of photoluminescence blinking in individual core/shell CdSe/CdS nanocrystals. *Nano Lett.* **11**, 5213–5218 (2011).
52. Mandel, L. Sub-Poissonian photon statistics in resonance fluorescence. *Opt. Lett.* **4**, 205–207 (1979).
53. Chung, I. & Bawendi, M. G. Relationship between single quantum-dot intermittency and fluorescence intensity decays from collections of dots. *Phys. Rev. B* **70**, 165304 (2004).
54. Chandrasekaran, V. et al. Nearly blinking-free, high-purity single-photon emission by colloidal InP/ZnSe quantum dots. *Nano Lett.* **17**, 6104–6109 (2017).
55. Takeuchi, H., Suzuku, S., Dianoux, A. J. & Allen, G. Low frequency vibrations in crystalline biphenyl: Model calculations and raman and neutron spectra. *Chem. Phys.* **55**, 153–162 (1981).
56. Ren, Z. Q., McNeil, L. E., Liu, S. & Kloc, C. Molecular motion and mobility in an organic single crystal: Raman study and model. *Phys. Rev. B* **80**, 245211 (2009).
57. Weinberg-Wolf, J. R., McNeil, L. E., Liu, S. & Kloc, C. Evidence of low intermolecular coupling in rubrene single crystals by Raman scattering. *J. Condens. Matter Phys.* **19**, 276204 (2007).
58. Yaffe, O. et al. Local polar fluctuations in lead halide perovskite crystals. *Phys. Rev. Lett.* **118**, 136001 (2017).
59. Pérez-Osorio, M. A. et al. Vibrational properties of the organic–inorganic halide perovskite $CH_3NH_3PbI_3$ from theory and experiment: factor group analysis, first-principles calculations, and low-temperature infrared spectra. *J. Phys. Chem. C.* **119**, 25703–25718 (2015).
60. Dahod, N. S., France-Lanord, A., Paritmongkol, W., Grossman, J. C. & Tisdale, W. A. Low-frequency Raman spectrum of 2D layered perovskites: local atomistic motion or superlattice modes? *J. Chem. Phys.* **153**, 044710 (2020).
61. Dhanabalan, B. et al. Directional anisotropy of the vibrational modes in 2D-layered perovskites. *ACS Nano* **14**, 4689–4697 (2020).
62. Hoffman, A. E. J. et al. Understanding the phase transition mechanism in the lead halide perovskite $CsPbBr_3$ via theoretical and experimental GIWAXS and Raman spectroscopy. *APL Mater.* **11**, 041124 (2023).
63. Rainò, G. et al. Ultra-narrow room-temperature emission from single $CsPbBr_3$ perovskite quantum dots. *Nat. Commun.* **13**, 2587 (2022).
64. Rainò, G. et al. Underestimated effect of a polymer matrix on the light emission of single $CsPbBr_3$ nanocrystals. *Nano Lett.* **19**, 3648–3653 (2019).
65. Nair, G., Zhao, J. & Bawendi, M. G. Biexciton quantum yield of single semiconductor nanocrystals from photon statistics. *Nano Lett.* **11**, 1136–1140 (2011).
66. de Mello Donegá, C., Bode, M. & Meijerink, A. Size- and temperature-dependence of exciton lifetimes in CdSe quantum dots. *Phys. Rev. B* **74**, 085320 (2006).
67. Ji, Z. & Song, Z. Exciton radiative lifetime in CdSe quantum dots. *J. Semicond.* **44**, 032702 (2023).

68. van Driel, A. F. et al. Frequency-dependent spontaneous emission rate from CdSe and CdTe nanocrystals: influence of dark states. *Phys. Rev. Lett.* **95**, 236804 (2005).
69. de Mello Donegá, C. & Koole, R. Size dependence of the spontaneous emission rate and absorption cross section of CdSe and CdTe quantum dots. *J. Phys. Chem. C.* **113**, 6511–6520 (2009).
70. Krieg, F. et al. Monodisperse long-chain sulfobetaine-capped $CsPbBr_3$ nanocrystals and their superfluorescent assemblies. *ACS Cent. Sci.* **7**, 135–144 (2021).
71. Oriel, E. H. et al. Intraband cooling and auger recombination in weakly to strongly quantum-confined $CsPbBr_3$ perovskite nanocrystals. *J. Phys. Chem. Lett.* **15**, 6062–6068 (2024).
72. Zhu, C. et al. Quantifying the size-dependent exciton-phonon coupling strength in single lead-halide perovskite quantum dots. *Adv. Opt. Mater.* **12**, 2301534 (2024).
73. Li, J., Gan, L., Fang, Z., He, H. & Ye, Z. Bright tail states in blue-emitting ultrasmall perovskite quantum dots. *J. Phys. Chem. Lett.* **8**, 6002–6008 (2017).
74. Boziki, A., Dar, M. I., Jacopin, G., Grätzel, M. & Rothlisberger, U. Molecular origin of the asymmetric photoluminescence spectra of $CsPbBr_3$ at low temperature. *J. Phys. Chem. Lett.* **12**, 2699–2704 (2021).
75. Fu, M. et al. Unraveling exciton–phonon coupling in individual $FAPbI_3$ nanocrystals emitting near-infrared single photons. *Nat. Commun.* **9**, 3318 (2018).
76. Tao, W., Zhang, C., Zhou, Q., Zhao, Y. & Zhu, H. Momentarily trapped exciton polaron in two-dimensional lead halide perovskites. *Nat. Commun.* **12**, 1400 (2021).
77. Atteberry, M. L., Mi, C., Chandra, S., Hidayatova, L. & Dong, Y. Unraveling the growth mechanism of strongly confined CsPbBr3 perovskite quantum dots under thermodynamic equilibrium control. *Chem. Mater.* **36**, 4521–4529 (2024).

Acknowledgements

This material is based upon work supported by the US Department of Energy, Office of Science, Basic Energy Science, under Award Number DE-SC0024441. This project is also supported in part by grants from the Research Council and the Dodge Family College of Arts and Science of the University of Oklahoma Norman Campus. We also acknowledge the support of the Vice President for Research and Partnerships at the University of Oklahoma. Y.S. is supported by the National Science Foundation via grant CHE-2102071. Use of the TAMU Materials Characterization Facility (RRID: SCR_022202) is acknowledged. This work was in part supported by the Trienens Institute for Sustainability and Energy at Northwestern University, and the NUFAB facility of Northwestern University's NUANCE Center, which has received support from the SHyNE Resource (NSF ECCS-2025633), the IIN, and Northwestern's MRSEC program (NSF DMR-2308691). We thank Dr. Sisi Xiang for their help with electron microscope image processing. We acknowledge Dr. Tian Qiao for her assistance with thin-film linear absorption measurements. We thank Dilruba Popy for her assistance in performing PXRD measurements. The DFT modeling was performed at the OU Supercomputing Center for Education and Research (OSCER) at the University of Oklahoma. The authors thank Dr. Robert B. Scafe and Dr. Clara Smith for their discussions on manuscript writing.

Author contributions

C.M. and G.C.G. performed the sample preparation, the optical spectroscopic experiments, and data processing; C.M. and Y.D. performed the data analyses; C.W.L., J.D.D., and Y.S. performed the DFT calculation and provided related discussions; D.S. and B.C. conducted the Raman spectroscopy experiments and provided related discussions; M.L.A., C.M., and L.H. performed the $CsPbBr_3$ QD syntheses; L.H. performed the $CsPbI_3$ QD syntheses; N.G.A. conducted the NMR and NOESY experiments and supported NMR data analyses; W.T.Y. supported the spectroscopic measurements; All authors contributed to manuscript writing; Y.D. supervised the project.

Competing interests

The authors declare no competing interests.

Additional information

Supplementary information The online version contains supplementary material available at https://doi.org/10.1038/s41467-024-55619-7.

Correspondence and requests for materials should be addressed to Yitong Dong.

Peer review information *Nature Communications* thanks the anonymous reviewer(s) for their contribution to the peer review of this work. A peer review file is available.